

HST Observations of HD 166620 and τ Ceti: First UV Spectra of a Magnetic Grand Minimum Star and the Extent of τ Ceti’s Astrophere⁵

Brian E. Wood², Hans-Reinhard Müller³, Dean Hartshorn⁴, Seth Redfield⁴, Travis S. Metcalfe⁵

ABSTRACT

We present new *Hubble Space Telescope* (HST) UV spectra of the K2 V star HD 166620, the first star clearly recognized to be in a “magnetic grand minimum” state analogous to the Sun’s “Maunder Minimum” in the late 1600’s. The stellar H I Lyman- α surface fluxes are extremely low, about a factor of two below fluxes observed during solar minimum, and also significantly lower than those of τ Ceti (G8 V) and HD 191408 (K2.5 V), two stars more similar to HD 166620 in spectral type and age (~ 10 Gyr) than the Sun. The τ Ceti data that are compared with HD 166620 include both old archival data and a new HST observation as well. The Lyman- α data are used to confirm a nondetection of astrospheric Lyman- α absorption for this star, suggesting a very weak wind with $\dot{M} < 0.1 \dot{M}_\odot$. The very compact astrosphere inferred for τ Ceti indicates that the star’s debris disk is at least partly exposed to the ISM, and we discuss possible consequences.

Subject headings: main sequence stars — stellar chromospheres — stellar winds — debris disks — interstellar absorption

1. Introduction

Our Sun has a well known 11-year activity cycle during which it alternates between periods of high activity, with lots of sunspots, active regions, and accompanying chromospheric and coronal activity; and periods of low activity, with no or few spots and active regions. This behavior is governed by the Sun’s internal magnetic dynamo, rooted in the Sun’s outer convection zone, where convective plasma motions influenced by differential rotation are generating magnetic fields

¹Based on observations made with the NASA/ESA Hubble Space Telescope, obtained at the Space Telescope Science Institute, which is operated by the Association of Universities for Research in Astronomy, Inc., under NASA contract NAS 5-26555. These observations are associated with program GO-17793.

²Naval Research Laboratory, Space Science Division, Washington, DC 20375, USA;
brian.e.wood26.civ@us.navy.mil

³Department of Physics and Astronomy, Dartmouth College, Hanover, NH 03755, USA

⁴Astronomy Department and Van Vleck Observatory, Wesleyan University, Middletown, CT 06459-0123, USA

⁵Center for Solar-Stellar Connections, WDRC, 9020 Brumm Trail, Golden, CO 80403, USA

(Charbonneau 2020). One avenue for exploring the nature of the activity cycle involves observing the cyclic behavior of other stars, which can be particularly important for inferring what the solar cycle may have been like in the past and what it might be like in the future.

Since stellar dynamos are driven in part by stellar rotation, the evolution of activity cycles over time will be tied to the evolution of stellar rotation. Stars begin their lives rotating rapidly, but this rotation slows with time due to a magnetic braking process whereby stellar winds drag against the large-scale field of the star, allowing stars to gradually shed angular momentum. The *Kepler* mission radically increased the number of stars with measured rotation periods, resulting in the surprising discovery that magnetic braking appears to slow or even shut down for old stars (van Saders et al. 2016, 2019; Hall et al. 2021; David et al. 2022). There is evidence that this weakened magnetic braking appears to be accompanied by an increasing activity cycle period, until a point where the activity cycle disappears entirely (Metcalfe & van Saders 2017; Metcalfe et al. 2022).

The Sun itself appears to be in this transitional state, lying above the relation between cycle period and rotation period established by younger stars with rotation rates that are still slowing. A glimpse into the Sun’s future as a non-cycling, flat-activity star is possibly provided by the “magnetic grand minimum” (MGM) phenomenon. During an MGM phase, the Sun’s activity cycle shuts down entirely. By far the most well known MGM is the “Maunder Minimum,” an extended period from roughly 1645–1715 when sunspots virtually disappeared (Eddy 1976; Usoskin et al. 2000), but other MGM periods have been identified over the last few millenia, using isotopic abundance proxies for sunspot number (Usoskin et al. 2021, 2025). It is possible that MGM phases are a direct symptom of weakened magnetic braking, and an activity cycle that is in the process of gradually disappearing (Metcalfe et al. 2025b).

A significant number of stars monitored for activity cycles have been found to have low, flat activity curves. These stars had originally been interpreted to possibly be in MGM states (Baliunas & Jastrow 1990), but most are now generally assumed to be inactive subgiants or very old main sequence stars with cycles that have simply disappeared entirely (Wright 2004; Metcalfe et al. 2022). Identifying a truly convincing MGM star requires monitoring for sufficiently long enough to discern clear cyclic behavior, followed by a clear cessation of that cyclic behavior for an extended period of time. This naturally requires many decades of observation. The first definitive MGM star appears to be the K2 V star HD 166620, which was observed to have a ~ 17 yr period from 1966–2004, but which has had low, flat activity for over 20 years since then (Baum et al. 2022; Luhn et al. 2022). Similar to our Sun, HD 166620 lies above the cycle-period/rotation-period relation defined by stars still experiencing full magnetic braking (Metcalfe et al. 2022), consistent with the hypothesis that MGM phases may be a phenomenon for stars with weakened magnetic braking, and are precursors to a complete shut down of the activity cycle.

We here present UV spectra of HD 166620 from the Space Telescope Imaging Spectrograph (STIS) instrument on board the *Hubble Space Telescope* (HST), in order to provide the first UV measurements for a star in an MGM state. These observations can hopefully provide some indica-

Table 1: HST/STIS Observations

Star	Start Time	Grating	Wavelengths (Å)	Exp. Time (s)
HD 166620	2025-05-18 08:15:32	E230H	2574–2851	1543
	2025-05-18 09:30:41	E140M	1150–1700	2629
τ Cet	2022-08-19 19:27:18	E230H	2574–2851	300
	2000-08-01 02:59:12	E140M	1150–1700	13450
HD 191408	2025-06-15 14:12:02	E140M	1150–1700	2093
	2018-09-04 12:12:30	E230H	2574–2851	306
	2018-09-04 10:55:44	E140M	1150–1700	4064

tion of what the Sun’s UV emission may have been like during its MGM phases, particularly the famous Maunder Minimum. However, there is a significant spectral type difference between the Sun and HD 166620. Thus, we will mostly be comparing our HD 166620 observations to spectra of τ Ceti (G8 V) and HD 191408 (K2.5 V), which are closer in size, mass, and spectral type to HD 166620. Like HD 166620, HD 191408 is a very old, inactive early K dwarf, where we will be taking advantage of a recently completed study of the star’s H I Lyman- α line from Youngblood et al. (2022). As for τ Ceti, it is an excellent example of an old, flat-activity star that has not shown a hint of an activity cycle since monitoring first began in the late 1960s (Baliunas et al. 1995; Baum et al. 2022). Thus, in comparing HD 166620 with τ Ceti, we will be comparing an MGM star with a temporarily halted activity cycle to a similar star that does not seem to have any cycle at all. For τ Ceti, we will not only utilize old, archival HST/STIS spectra, but we have also obtained more recent HST data that can be presented here for the first time.

2. HST Observations

The UV emission lines that we will be focusing on are primarily the H I Lyman- α (Ly α) line at 1215.7 Å and the Mg II h & k lines at 2803.5 Å and 2796.3 Å, respectively. These are the strongest chromospheric lines available in the UV, and as such are the best diagnostics of chromospheric activity. Table 1 lists the HST/STIS observations considered here, consisting of both new and archival data. These spectra include near-UV (NUV) spectra of the 2574–2851 Å spectral region with the E230H grating, providing the highest possible spectral resolution of the Mg II lines, and far-UV (FUV) spectra of the 1150–1700 Å region with the moderate resolution E140M grating.

As shown in Table 1, the E230H and E140M spectra of HD 166620 are recent observations from 2025 May 18. In the same observing program, we obtained a new τ Ceti E140M spectrum on 2025 June 15, though we will also be considering the older E140M and E230H spectra from 2000 August 1 and 2022 August 19, respectively. Table 1 also lists E230H and E140M spectra of the K2.5 V star HD 191408 from 2018 September 4, as the Ly α and Mg II lines of this star will also be utilized, for reasons that will be made clear in the next section. All spectra were initially processed using the standard HST/STIS CALSTIS software, though as we will discuss in detail in

Table 2: Stellar Properties

Star	Spect. Type	Dist. (pc)	Radius (R_{\odot})	V_{rad} (km s^{-1})	P_{rot} (days)	P_{cyc} (yrs)	[Fe/H]	[Mg/H]	[C/H]	Age (Gyr)	Refs
τ Cet	G8 V	3.65	0.793	-16.6	46	flat	-0.52	-0.25	-0.39	9.0 ± 1.0	1, 2, 3, 4
HD 191408	K2.5 V	6.01	0.744	-129.3	-0.47	-0.09	-0.39	9–14	4, 5, 6
HD 166620	K2 V	11.1	0.782	-19.3	45	17	-0.10	0.11	-0.19	$9.5_{-1.65}^{+2.15}$	2, 4, 7, 8

References — (1) Korolik et al. (2023); (2) Baum et al. (2022); (3) Tang & Gai (2011); (4) Allende Prieto et al. (2004); (5) Youngblood et al. (2022); (6) Ghezzi et al. (2010); (7) Metcalfe et al. (2025a); (8) Luhn et al. (2022).

Section 4, modifications to the data reduction were found necessary to properly extract some of the weaker lines in the E140M spectra.

Table 2 lists basic stellar properties that we will be assuming. The listed spectral types, distances, and radial velocities (V_{rad}) are from the SIMBAD database. Photospheric abundances from Allende Prieto et al. (2004) are listed for three elements: [Fe/H], [Mg/H], and [C/H]. Following convention, the abundances are listed as logarithmic values relative to solar, so a value of zero would imply a solar abundance. The activity cycle periods, P_{cyc} , are from Baum et al. (2022). Korolik et al. (2023) provide a recent reassessment of τ Ceti’s properties, which is our source for the stellar radius and rotation period (P_{rot}) of this star, though τ Ceti’s pole-on orientation makes it very difficult to infer an unambiguous rotation period despite extensive photometric monitoring. For HD 166620, P_{rot} is from Luhn et al. (2022). The stellar radii of HD 191408 and HD 166620 are from Youngblood et al. (2022) and Metcalfe et al. (2025a), respectively. The estimated ages of the three stars are from Tang & Gai (2011), Ghezzi et al. (2010), and Metcalfe et al. (2025a). For τ Ceti, the quoted stellar age (9.0 ± 1.0 Gyr) is from asteroseismology (Tang & Gai 2011). For HD 191408, we follow Youngblood et al. (2022) in using the isochrone-derived 9–14 Gyr age range from Ghezzi et al. (2010). For HD 166620, we assume $9.5_{-1.65}^{+2.15}$ Gyr based on gyrochronology, but with correction for weakened magnetic braking. All of our stars are old stars with ages of about 10 Gyr. It is worth mentioning that all three have very low X-ray luminosities, with $\log L_X < 27.0$ measured by ROSAT (e.g., Schmitt & Liefke 2004), consistent with old age.

3. Interstellar Absorption Analysis

Figure 1 shows the H I Ly α lines of our three target stars. For τ Ceti, both the old spectrum from 2000 and the new one from 2025 are shown. Using the distances and stellar radii listed in Table 2, the observed fluxes have been converted to surface fluxes. The Ly α line profiles are complicated by extensive ISM absorption. The Sun lies within a partly neutral cloud called the Local Interstellar Cloud (LIC), so even for the nearest stars the Ly α absorption from the ISM is strong and very broad, typically centered within $\sim 30 \text{ km s}^{-1}$ of the heliocentric rest frame. The ISM also produces narrow deuterium (D I) absorption -81.6 km s^{-1} from the H I absorption. The location of the D I absorption is explicitly indicated in Figure 1.

Finally, there is also geocoronal Ly α emission present in the data. This narrow emission is indicated by the shaded regions in Figure 1, mostly contained in the saturated core of the ISM H I absorption, making it easy to remove by fitting a Gaussian to the emission and then subtracting the Gaussian. The geocoronal emission should be centered on the Earth’s projected velocity toward the observed star, which is known. Thus, this emission is actually an excellent wavelength calibrator, and we correct the wavelength scale of our spectra accordingly (see Wood et al. 2005b). Note that for HD 191408 the geocoronal emission is only faintly visible at about -23 km s^{-1} . It is very weak because this spectrum was taken through the narrow $0.2'' \times 0.06''$ slit instead of the more standard $0.2'' \times 0.2''$ aperture. This suppresses the geocoronal emission significantly, and improves spectral resolution somewhat, but it does mean the flux calibration will be more uncertain, which could be a concern for our purposes.

We are mostly interested in the intrinsic stellar Ly α fluxes and the intrinsic line profiles, but inferring these from the spectra in Figure 1 requires correcting for the ISM absorption. This is somewhat easier for HD 191408 than for the other two stars due to the large radial velocity ($V_{rad} = -129.3 \text{ km s}^{-1}$), which blueshifts the stellar emission away from the ISM rest frame. This is a major reason why we have included HD 191408 in our study. Not only is this star similar in spectral type to HD 166620 and τ Ceti, and with a similar old age of about 10 Gyr, but the left half of the stellar profile is relatively free of ISM absorption. The Ly α line for HD 191408 has already been reconstructed by Youngblood et al. (2022), a reconstruction that should be somewhat more accurate than the ones we will do for τ Ceti and HD 166620, with more obscured line profiles.

With Wood et al. (2005b) and Youngblood et al. (2022) already having analyzed the old τ Ceti and HD 191408 spectra, respectively, we here focus on HD 166620 and the new τ Ceti spectrum. Before tackling Ly α , it is useful to learn more about the ISM velocity structure by analyzing the much narrower ISM Mg II and Fe II absorption lines in the high resolution E230H spectra. Nisak et al. (2025) have already analyzed the τ Ceti lines, allowing us to focus on HD 166620. Figure 2 shows the ISM Mg II and Fe II absorption lines observed toward HD 166620.

We fit these lines as in past analyses (e.g., Redfield & Linsky 2002, 2004; Nisak et al. 2025). Each absorption component is defined by three parameters: the central velocity (v), Doppler broadening parameter (b), and column density (N). Before comparing a model absorption profile with the data, it is convolved with the instrumental line spread function (Medallion et al. 2023). Although the evidence is subtle, it is clear that there are at least two ISM velocity components present in the absorption. Each of the two Mg II lines is fitted independently, and then the two lines are fitted simultaneously with parameters forced to be self-consistent. In each case, the best two-component fit is determined by χ^2 minimization, with uncertainties in the fit parameters estimated using a Monte Carlo technique. This provides three separate measurements of the ISM absorption. The final Mg II fit parameters reported in Table 3 are a weighted mean of the three independent measurements, though the fit shown in Figure 2 is the simultaneous fit to both lines. The two Fe II ISM lines are similarly analyzed, with results also shown in Figure 2 and Table 3. The τ Ceti Mg II and Fe II line parameters measured by Nisak et al. (2025) are listed in Table 3 as well. Only one

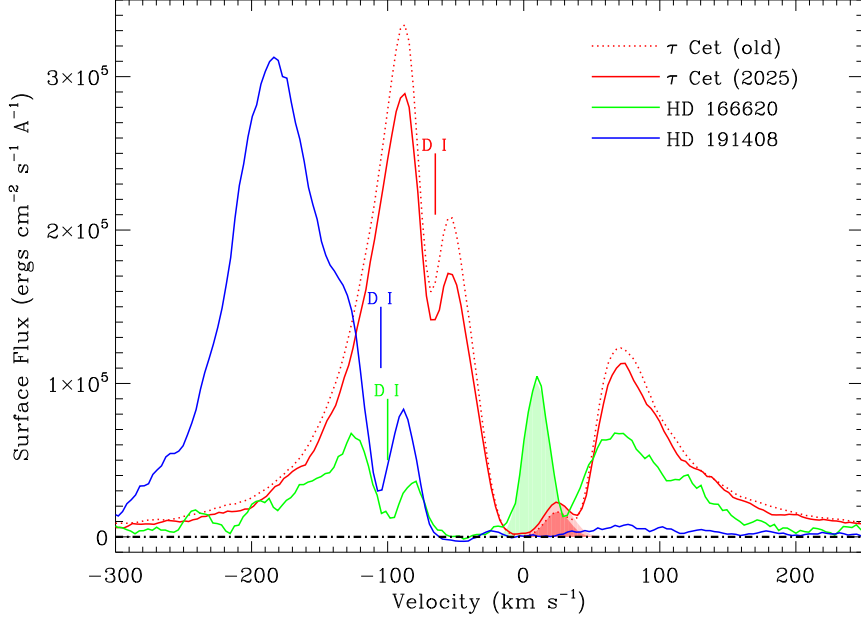


Fig. 1.— Slightly smoothed HST/STIS spectra of the H I Ly α line of three stars, plotted in surface flux units on a heliocentric velocity scale. Two separate spectra are shown for τ Ceti. Very broad H I ISM absorption absorbs the central part of the line profile, with narrow D I absorption also being present blueward of H I. Shaded regions indicate narrow geocoronal emission within the saturated core of the H I absorption.

velocity component is observed toward τ Ceti.

Turning our attention to fitting Ly α , the Mg II and Fe II lines assist in the H I Ly α analyses in a couple ways. Besides providing information about the ISM velocity structure, which cannot be discerned in the much broader H I and D I lines, once the ISM absorption is removed the Mg II lines provide an excellent first guess for the intrinsic stellar H I Ly α profile. Both Ly α and Mg II h & k are very strong chromospheric lines, with similar profiles in solar spectra. The self-reversal seen at the center of the Mg II lines in Figure 2 is typical of these lines (Taylor et al. 2024). For the narrow ISM Mg II and Fe II lines, it is possible to infer a stellar background by simple interpolation (see Figure 2), but this is definitely not possible for Ly α . For Ly α , the basic idea is to use the Mg II k line profile as a first guess for the shape of the stellar profile. An initial fit to the ISM absorption is then performed. Residuals of that fit are used to adjust the assumed shape of the background stellar profile, followed by a new fit to the ISM absorption. Figure 3 shows our best Ly α fits after a couple iterations of this. These are for the new τ Ceti spectrum from 2025, and the HD 166620 spectrum.

Both H I and D I lines are fitted simultaneously, taking into account the two fine-structure constituents of the lines (see Table 3), and forcing the H I and D I lines to have self-consistent velocities and Doppler parameters. With H I and D I being dominated by thermal broadening,

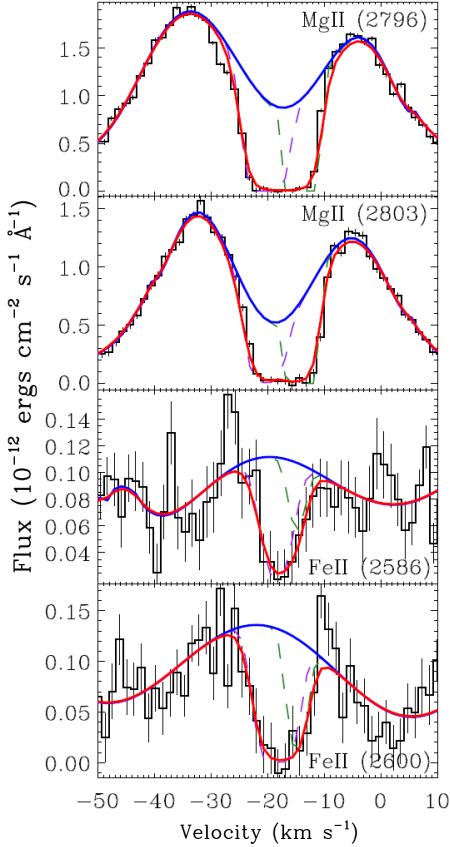


Fig. 2.— HST/STIS spectra of ISM Mg II and Fe II absorption lines observed toward HD 166620, plotted on a heliocentric velocity scale. Blue lines indicate the assumed stellar background above the absorption. The absorption profiles are fitted with two components (dashed lines), with the red line being the combination of the two after instrumental smoothing, which fits the data.

the latter constraint means $b(\text{HI}) = \sqrt{2} \times b(\text{DI})$. We also simply assume a D/H ratio of $D/\text{H} = 1.56 \times 10^{-5}$, a value that has been found to apply throughout the nearby ISM (Wood et al. 2004). In this manner, the three fit parameters of each H I absorption component are entirely dependent on the D I parameters. Thus, in a single-component fit to the data, as is the case for τ Ceti, there are actually only three free parameters to the entire H I+D I absorption fit, and in Table 3 we therefore only list the H I parameters.

For HD 166620, there are two ISM components, and we take this into account in the Ly α analysis. Because the two components are completely blended in H I and D I, we use the Fe II parameters to constrain the Ly α fit. We use Fe II instead of Mg II because the Mg II absorption for HD 166620 is saturated (see Figure 2), leading to larger uncertainties in the fit parameters. In our Ly α fit, we assume the velocity separation and column density ratio are the same for H I+D I as observed for Fe II, and we simply assume both components have the same Doppler parameter. In this way, even the two-component HD 166620 Ly α fit has only three free parameters, and in Table 3 we use parentheses to indicate that the second ISM component's parameters are not inferred independently.

Table 3: ISM Absorption Measurements^a

Star	Ion	λ_{rest}^b (Å)	ISM Cloud	v^c (km s ⁻¹)	b (km s ⁻¹)	$\log N$ $\log(\text{cm}^{-2})$
HD 166620	Mg II	2796.3543, 2803.5315	Mic	-20.44 ± 0.70	2.64 ± 0.17	12.98 ± 0.13
	Mg II	2796.3543, 2803.5315	LIC	-14.19 ± 0.46	1.66 ± 0.18	13.92 ± 0.28
	Fe II	2586.6500, 2600.1729	Mic	-18.47 ± 0.10	3.25 ± 0.51	$13.245^{+0.053}_{-0.060}$
	Fe II	2586.6500, 2600.1729	LIC	-14.81 ± 0.27	1.61 ± 0.50	12.744 ± 0.067
	H I	1215.6682, 1215.6736	Mic	-19.84 ± 0.97	13.03 ± 1.42	18.235 ± 0.021
	H I	1215.6682, 1215.6736	LIC	(-16.19 ± 0.97)	(13.03 ± 1.42)	(17.734 ± 0.021)
τ Cet (old) ^d	Mg II	2796.3543, 2803.5315	LIC?	13.26 ± 0.46	3.07 ± 0.62	13.12 ± 0.40
	Fe II	2586.6500, 2600.1729	LIC?	14.29 ± 0.15	1.70 ± 0.37	12.92 ± 0.70
	H I	1215.6682, 1215.6736	LIC?	12.34 ± 0.06	10.32 ± 0.06	18.006 ± 0.002
τ Cet (2025)	H I	1215.6682, 1215.6736	LIC?	12.59 ± 0.14	10.20 ± 0.19	18.066 ± 0.005

Notes — ^aValues in parentheses are fixed relative to other component (see text). ^bRest wavelengths of measured lines, in vacuum. ^cCentral velocity in a heliocentric rest frame. ^dFrom Wood et al. (2005b) and Nisak et al. (2025).

In a number of past analyses, we have sometimes found that we cannot fit the H I and D I absorption in a self-consistent manner without including an extra H I absorption component that is interpreted as being heliospheric and/or astrospheric in origin, associated with solar/stellar wind interactions with the ISM (Wood et al. 2005b, 2021). We see no evidence for such extra H I absorption for τ Ceti or HD 166620 (see Figure 3), and Youngblood et al. (2022) found no evidence for such absorption for HD 191408 either.

Figure 1 provides a direct comparison of two separate H I Ly α spectra for τ Ceti. There is little apparent difference between the two, though fluxes are slightly lower for the new 2025 spectrum. The old spectrum was analyzed by Wood et al. (2005b), and we have here analyzed the new spectrum. These independent analyses provide an excellent opportunity to assess the uncertainties in the ISM fit parameters. The formal uncertainties in Table 3 are associated with the random errors induced by the noise in the data, as determined by Monte Carlo modeling. However, systematic errors probably dominate, particularly for the Ly α fits, where uncertainties in the background stellar profile will be large. The H I velocities of $v = 12.34 \pm 0.06$ km s⁻¹ and $v = 12.59 \pm 0.14$ km s⁻¹ are in reasonably good agreement, consistent with the expected accuracy of the wavelength calibration. Since we are using the geocoronal emission as a wavelength calibrator, this accuracy is defined by how well the centroid of the geocoronal emission can be measured. For the noisier 2025 spectrum, the estimated uncertainty based on the Gaussian fit to the emission is ± 0.5 km s⁻¹. The Doppler parameters of $b = 10.32 \pm 0.06$ km s⁻¹ and $b = 10.20 \pm 0.19$ km s⁻¹ are in very good agreement. As for column density, the two measured τ Ceti values from Table 3 are $\log N(H) = 18.006 \pm 0.002$ and $\log N(H) = 18.066 \pm 0.005$. There is a significant 0.06 dex difference between the two, which is much larger than the random error estimates, and is presumed to be due to uncertainties in the reconstructed stellar Ly α profile. We will return to this issue in

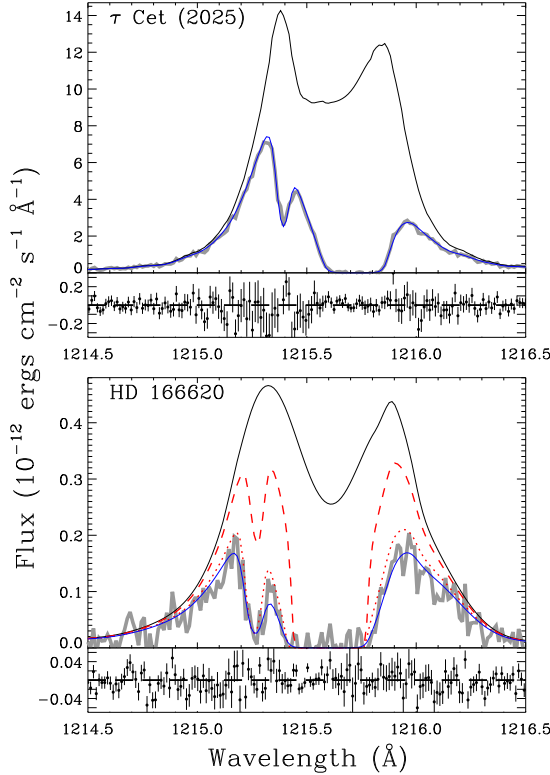


Fig. 3.— Fits to the H I Ly α lines of τ Ceti (for the 2025 spectrum) and HD 166620, with residuals shown underneath. Solid black lines are the inferred intrinsic stellar line profile, and blue lines indicate the ISM absorption line fit to the data. Only a single ISM component is assumed for τ Ceti, while two are assumed for HD 166620 (red lines), where the Fe II fit from Figure 2 is used to constrain the two-component fit.

Section 5.

Although we are mostly interested in the chromospheric Mg II and Ly α line fluxes, corrected for ISM absorption, the ISM absorption itself is of some interest, so we here provide some discussion of the ISM measurements. For each detected ISM component in Table 3, we have used the cloud radial velocities and local ISM maps from Redfield & Linsky (2008) to identify likely nearby clouds responsible for the absorption, and these are listed in the fourth column of Table 3. Starting with the HD 166620 line of sight (LOS), the two components are likely identified with the Mic cloud, with a predicted velocity toward HD 166620 of $v = -19.82 \text{ km s}^{-1}$, and the LIC that surrounds the Sun, with a predicted velocity of $v = -13.35 \text{ km s}^{-1}$.

The simpler, single-component τ Ceti LOS is potentially intriguing, as there is ambiguity about whether we are seeing absorption from the LIC, which surrounds the Sun, or the adjacent G cloud. Although the Sun is located within the LIC, it appears to be very near the edge of it, with the G cloud located on the other side. The predicted LIC and G cloud velocities toward τ Ceti are $v = 11.7 \text{ km s}^{-1}$ and $v = 17.7 \text{ km s}^{-1}$, respectively (Redfield & Linsky 2008). The Mg II and Fe II

Table 4: Surface Flux Measurements

Star	Surface Fluxes (10^3 ergs cm^{-2} s^{-1})			
	H I Ly α	Mg II h+k	C II λ 1335	C IV λ 1548
HD 166620	161 ± 16	522 ± 21	1.06 ± 0.18	1.67 ± 0.29
τ Cet (old)	405 ± 41	743 ± 30	1.84 ± 0.03	1.87 ± 0.04
τ Cet (2025)	394 ± 39	...	1.54 ± 0.05	1.46 ± 0.09
HD 191408 ^a	259 ± 26	545 ± 22	0.68 ± 0.04	0.77 ± 0.07
Sun (minimum) ^b	271	1552

Notes — ^aFlux calibration potentially uncertain due to use of the narrow $0.2'' \times 0.06''$ aperture. ^bSolar minimum values from Lean et al. (2022).

velocities are in between the two, suggesting there may be a mixture of the two along the LOS (Nisak et al. 2025). This is consistent with the recently expressed view that the Sun is near or within a compression region that could be described as being due to a collision between the G and LIC clouds, possibly associated with a supernova shell (Swaczyna et al. 2022; Zucker et al. 2025; Youngblood et al. 2025).

We here note that the ISM temperature suggested by the H I Doppler parameter is intermediate between the G and LIC clouds, and the depletion values for Mg and Fe are intermediate as well, consistent with a mixed LOS. The temperature suggested by the $b(H) = 10.32 \pm 0.06$ km s^{-1} measurement from Table 3 for the older data is 6435 ± 75 K, assuming purely thermal broadening. This is between the $T = 7500 \pm 1300$ K and $T = 5500 \pm 400$ K values for the LIC and G clouds, respectively (Redfield & Linsky 2008). If we assume the average $\log N(H) = 18.04$ value from the two τ Ceti measurements, and solar abundances from Asplund et al. (2009), the Mg and Fe column densities from Table 3 suggest ISM dust depletions of $D(\text{Mg}) = -0.52 \pm 0.40$ and $D(\text{Fe}) = -0.62 \pm 0.70$. The quoted uncertainties are large, but these measurements are also between the expected LIC and G values: Redfield & Linsky (2008) quote LIC and G values of $D(\text{Mg}) = -0.97 \pm 0.23$ and $D(\text{Mg}) = -0.36 \pm 0.35$, respectively, and $D(\text{Fe}) = -1.12 \pm 0.10$ and $D(\text{Fe}) = -0.54 \pm 0.11$, respectively. With the G cloud being less dust depleted than the LIC, a mixture of LIC and G cloud absorption might also explain why the Mg II and Fe II velocities are shifted more toward the G cloud velocity ($v = 17.7$ km s^{-1}) than H I (and D I).

4. Chromospheric Line Fluxes

With the Mg II and H I Ly α lines corrected for ISM absorption, we can now measure chromospheric line fluxes from them. Figure 4 compares the H I and Mg II line profiles of τ Ceti, HD 166620, and HD 191408; with integrated line fluxes reported in Table 4. The fluxes are displayed and listed in surface flux units assuming the stellar distances and radii listed in Table 2. The reported Mg II fluxes are for the sum of the h and k lines. Estimating uncertainties for Ly α fluxes is difficult, since the uncertainty is dominated by the large correction for ISM absorption (see

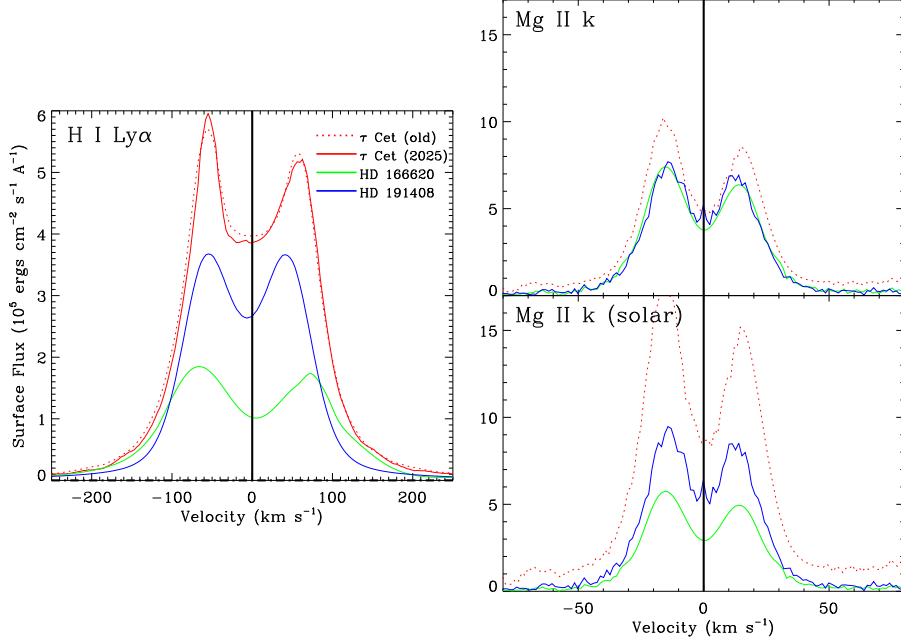


Fig. 4.— The H I Ly α and Mg II k lines of our three G8-K2 dwarf stars, plotted in surface flux units versus a velocity scale in the stellar rest frame. The bottom panel of the Mg II figure shows the spectra after normalization to a solar Mg abundance.

Figure 3). The new τ Ceti data provide an opportunity to assess this. Our analysis of the 2025 τ Ceti spectrum has yielded an inferred stellar Ly α profile and line flux in very good agreement with the previous analysis of the older E140M spectrum (see Figure 4). This is both encouraging for the accuracy of the stellar profile reconstruction, and also is illustrative of just how steady τ Ceti’s UV line fluxes are, consistent with the star being a prototypical flat activity star (Baum et al. 2022). Nevertheless, even for nearby stars with modest ISM absorption flux corrections we expect Ly α flux uncertainties of at least 10%, so the uncertainties reported in Table 4 simply assume this uncertainty level. For Mg II, flux uncertainties from noise in the spectra are extremely low, so in Table 4 we instead quote 4% uncertainties based on estimates of flux calibration uncertainties for STIS/E230H spectra (Hernandez et al. 2024).

A central goal of this study is to compare the chromospheric line profiles and fluxes for very old, inactive G8-K2 V stars. The inferred Ly α line profiles of our three stars are similar, with similar inferred self reversals near line center, but we do see significant differences in Ly α line flux in Figure 4. Our MGM star, HD 166620, appears to have a particularly low flux. The only G8-K3 V stars that we could find that might have Ly α surface fluxes this low measured from HST spectra are Kepler 444 (Bourrier et al. 2017; Linsky et al. 2020) and Ross 825 (Schneider et al. 2019). These are also clearly very old ~ 10 Gyr stars, but these are lower spectral resolution observations toward more distant targets, with correspondingly larger uncertainties. Thus, our quoted Ly α surface flux of $F_{Ly\alpha} = (1.61 \pm 0.16) \times 10^5$ ergs cm^{-2} s^{-1} is a plausible estimate of the true minimum value for

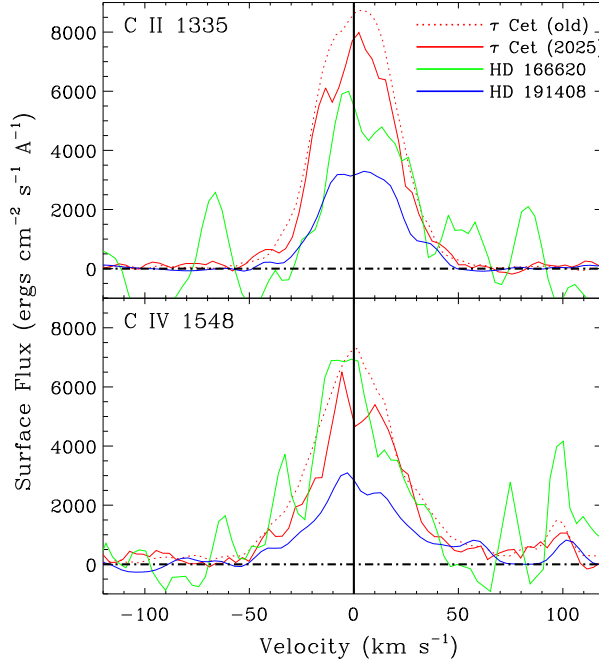


Fig. 5.— Slightly smoothed spectra of the C II 1335.692 Å and C IV 1548.204 Å lines of our three G8-K2 dwarf stars, plotted in surface flux units versus a velocity scale in the stellar rest frame.

G8-K2 dwarf stars. This can be compared with the solar minimum value of $F_{Ly\alpha} = 2.71 \times 10^5$ ergs cm $^{-2}$ s $^{-1}$ from Lean et al. (2022), which is roughly what we see for HD 191408.

In contrast to H I Ly α , the Mg II fluxes seen from our three target stars are nearly identical (see Figure 4). However, this consistency may be misleading, as these stars have different metallicities, with τ Ceti and HD 191408 being metal poor but HD 166620 being closer to solar metallicity. The bottom right panel of Figure 4 shows the Mg II lines corrected to solar abundances based on the [Mg/H] abundances listed in Table 2. With this correction, we recover a flux progression similar to that seen for Ly α , with fluxes increasing from HD 166620 to HD 191408 to τ Ceti. This exercise serves to illustrate one major advantage of Ly α as a chromospheric diagnostic, which is that this emission is from the dominant atomic constituent, hydrogen, and interpretation of Ly α fluxes is therefore not complicated by abundance issues.

The H I Ly α and Mg II h & k lines are by far the strongest chromospheric diagnostics available in our UV spectra, emanating from plasma with temperatures of $\log T = 4.0 - 4.3$. In order to measure activity at higher temperatures, in the so-called transition region (roughly $4.5 < \log T = 5.5$), we also measure line fluxes for the C II line at 1335.692 Å, and the C IV line at 1548.204 Å. The C II and C IV lines are much weaker than Ly α and Mg II, and for HD 166620 and HD 191408 are observed at very low signal-to-noise (S/N). The weaker member of the C IV doublet at 1550.781 Å is in fact undetected, although this is largely because it is in a different echelle order than the 1548.204 Å line, where the detector background is much higher. The C II line at 1334.519 Å is clearly seen for all our stars, but it is often affected by ISM absorption, so we focus only on the

C II 1335.692 Å line.

The E140M spectrum of HD 191408 is a coaddition of two exposures from two successive HST orbits, and comparison of the two exposures reveals a potential problem with data reduction of low S/N HST echelle spectra. The spectrum extracted from the first exposure (dataset odn902010) shows a clear C IV line, but this is not the case for the second exposure (dataset odn902030). Inspection of the echelle image of odn902030 clearly shows C IV emission that the standard data reduction is failing to extract. We note that the detector background is significantly higher for odn902030 than for odn902010, indicating that this high background may be responsible for the spectral extraction problems.

Further study indicates that the standard CALSTIS “x1d” spectral processing, which involves cross-correlation to optimally locate the individual echelle orders, can fail when the stellar spectrum is weak and contains only a few faint emission lines. This is especially true when the raw echellegrams are dominated by MAMA glow and point-like hot pixels and particle hits. For this reason, a new set of extractions was performed for the low S/N HD 166620 and HD 191408 E140M data using a fixed global template of order y-locations, adjusted to match the prominent Ly α feature in order 122 in each exposure, and employing the standard order traces (“1dt” file), slit height (7 pixels), and flanking background extraction widths (5 pixels). The default scattered-light correction was disabled, as it provides an unfiltered background trace that can corrupt the net spectrum if there are strong particle spikes, and instead a median-filtered and boxcar-smoothed background was applied to avoid introducing spurious background artifacts into the spectrum itself. The new extractions show good agreement between the O I, C II, and C IV features of the separate exposures of HD 191408, whereas the archive-processed x1d spectra completely misses C IV 1548 in the second observation, despite being clearly visible in the raw image. The strong Ly α line is not affected at all by this revised processing.

The C II and C IV line profiles are shown in Figure 5, and the fluxes are listed in Table 4, where in this case the quoted uncertainties are simply those associated with the noise in the spectra. For τ Ceti, we find C II and C IV fluxes that are 15%–20% lower in 2025 than they were in the older 2000 spectrum, representing a significantly larger change than observed for Ly α . Thus, even the flat-activity τ Ceti exhibits some degree of UV variability, particularly for higher temperature lines. Note that Judge et al. (2004) and Ayres et al. (2022) provide more detailed studies of the high-quality τ Ceti transition region line profiles.

Surprisingly, for C II and C IV the star with the lowest fluxes seems to be HD 191408, instead of HD 166620 (see Figure 5). We could normalize the fluxes to solar C abundances, based on the [C/H] abundances listed in Table 2, analogous to what is done in Figure 4 for Mg II. This mitigates the effect somewhat, but we still find HD 191408 C II and C IV fluxes that are particularly low. There is some reason for concern about the flux calibration of the HD 191408 E140M spectrum, because it was taken through the narrow $0.2'' \times 0.06''$ aperture instead of the more standard and photometric $0.2'' \times 0.2''$ aperture. Nevertheless, the H I Ly α fluxes shown in Figures 1 and 4 seem

reasonable for HD 191408, and are identical for the two aforementioned separate E140M exposures of this star.

Interestingly enough, it is τ Ceti that seems to be the faintest of the three stars in coronal X-rays, if measurements from ROSAT’s High Resolution Imager (HRI) are the guide. The two ROSAT/HRI exposures of τ Ceti imply $\log L_X = 26.37$ and $\log L_X = 26.54$ (in ergs s^{-1}), while for HD 166620 and HD 191408 ROSAT/HRI measures $\log L_X = 26.96$ and $\log L_X = 26.82$, respectively (Schmitt & Liefke 2004). The HD 166620 HRI observation is from October 1996, when the star was last at an activity cycle maximum (Luhn et al. 2022). In any case, for our three stars it is curious that it is τ Ceti that seems the least active coronally, HD 191408 that is least active in the transition region, and HD 166620 that is least active in the chromosphere.

Does the particularly low Ly α flux of HD 166620 in Figure 4 imply that stars in MGM phases have chromospheric fluxes that are very low even compared to stars at activity cycle minima? This question is of particular interest because there has in the past been speculation about what effects solar MGM phases might have had on Earth’s climate. The Maunder Minimum has been hypothesized to have contributed to the “Little Ice Age” period on Earth, though the much longer duration of the Little Ice Age casts doubt on this connection (Owens et al. 2017). A lack of direct measurement of solar radiative output during the Maunder Minimum prevents any definitive determination of whether any solar radiative changes might have affected Earth’s atmosphere significantly.

There is potential for UV variability to have an outsized effect on climate due to its effects on the chemistry of Earth’s upper atmosphere. Attempts to extrapolate radiative correlations observed in modern times to the Maunder Minimum suggest that H I Ly α fluxes might have been of order 5%–10% lower than solar minimum values (Krivova et al. 2010; Wu et al. 2018). In contrast, our HD 166620 Ly α flux is about 40% lower than a typical solar minimum value, suggesting lower $F_{Ly\alpha}$ is at least possible.

A true test of whether an MGM phase significantly reduces $F_{Ly\alpha}$ would require an HD 166620 Ly α measurement during a typical activity cycle minimum phase for this star, to compare with the MGM value that we measure here. Unfortunately, such a measurement is not available, meaning that it is entirely possible that HD 166620 simply has a particularly low $F_{Ly\alpha}$ whenever it is in a low activity state. The Ca II H & K monitoring of the star would seem to support this, as the Ca II S-index during its current flat-activity phase is *not* lower than observed during minima of its former cycling period (Baum et al. 2022; Luhn et al. 2022). We have looked at the *International Ultraviolet Explorer* (IUE) archive to see what Mg II measurements IUE could provide, but the only relevant observation is a single LWR-HI spectrum from 1983 July 7, which provides a surface flux measurement of $F_{MgII} = 6.3 \times 10^5 \text{ ergs cm}^{-2} \text{ s}^{-1}$, about 20% higher than the STIS value in Table 4. In 1983, HD 166620 was nearing a magnetic minimum but was not quite there (Luhn et al. 2022), so a slightly higher Mg II flux in 1983 is consistent with expectations.

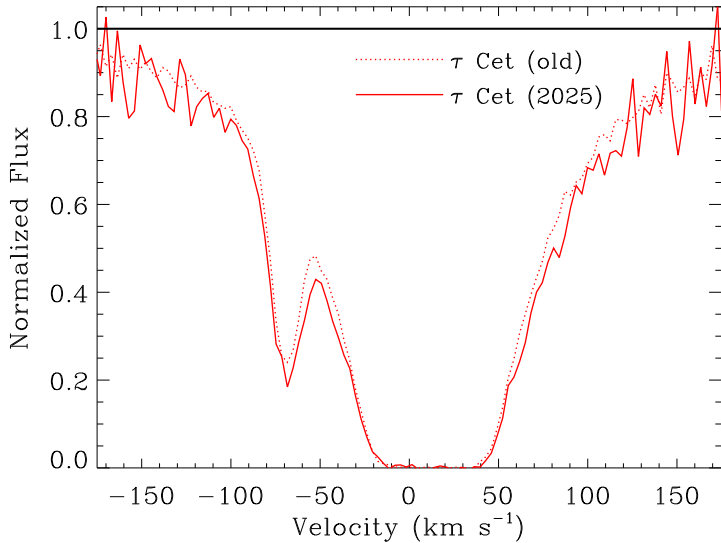


Fig. 6.— Comparison of ISM absorption profiles inferred for the H I+D I Ly α line of τ Ceti based on independent analyses of both the original STIS/E140M spectrum from 2000, and the new STIS/E140M spectrum from 2025. The spectrum is plotted on a heliocentric rest frame.

5. Implications of a Weak τ Ceti Wind

5.1. Astropheric Implications

One aspect of our study is a comparison of two Ly α spectra of τ Ceti, the older one having been first analyzed by Wood et al. (2005b), and the new one independently analyzed here (see Figure 3). In both cases we are able to fit the data with only ISM absorption, with no evidence for significant absorption contributions from the stellar astrosphere or our own heliosphere, as is sometimes seen toward nearby stars (Wood et al. 2005b, 2021). Though undetected, there should in principle be some astrospheric absorption present on the blue side of the H I ISM absorption profile. In comparing our two Ly α spectra taken 25 years apart, we look for very subtle changes in the Ly α absorption profile that might be indicative of variation in this weak, undetected astrospheric absorption. In Figure 6, we directly compare the inferred H I+D I absorption profiles for the two τ Ceti spectra. Our analysis suggests slightly stronger absorption for the 2025 data than for the old spectrum, with a correspondingly higher inferred $\log N(H)$ value (see Table 3).

Is it possible that the higher $\log N(H)$ value for the new 2025 spectrum could actually be due to a slight increase in this very weak astrospheric absorption? This is doubtful, as such an increase should also result in a slight blueshift of the H I absorption, since the blue side of the H I absorption is where the astrospheric absorption would reside (Wood et al. 2005b, 2021). We see no evidence of such a blueshift, so we interpret the absorption difference in Figure 6, and the associated 0.06 dex discrepancy in $\log N(H)$, as being indicative of systematic errors induced by uncertainties in the stellar Ly α line profile, which the random uncertainties quoted in Table 3 fail to quantify.

Because τ Ceti is so nearby ($d = 3.65$ pc), it is almost certainly surrounded by partially neutral

ISM analogous to that which surrounds the Sun. This kind of ISM clearly dominates within about 7 pc of the Sun, as opposed to the completely ionized ISM that predominates within the Local Bubble as a whole (Wood 2018; Wood et al. 2021). Therefore, the most likely reason for the nondetection of astrospheric absorption for τ Ceti is simply that its stellar wind is too weak to create a detectable astrosphere. The nondetection of astrospheric absorption can therefore be used to infer a meaningful upper limit for the stellar mass loss rate. This has already been done, with an inferred upper limit of $\dot{M} < 0.1 \dot{M}_\odot$, where the solar mass loss rate is roughly $\dot{M}_\odot = 2 \times 10^{-14} \text{ M}_\odot \text{ yr}^{-1}$ (Wood 2018). This is in fact the weakest wind yet inferred from any astrospheric absorption analysis (Wood et al. 2021). The particularly low upper limit implies that the τ Ceti astrosphere should in principle have been quite detectable, if the stellar wind was anywhere near as strong as the solar wind. The expected detectability is in part due to the relatively low ISM H I column density (and correspondingly narrow ISM absorption). But also very important is the high ISM speed of $V_{ISM} = 56 \text{ km s}^{-1}$ seen by the star, which increases the heating and deceleration of the ISM H I as it piles up against the astropause, which should in turn increase the amount of astrospheric absorption seen blueward of the ISM absorption.

The original astrospheric analysis for τ Ceti was actually done using hydrodynamic models previously computed for a different star, 61 Vir, with a similar $V_{ISM} = 51 \text{ km s}^{-1}$ value (Wood 2018). There is value in redoing this analysis with brand new models computed specifically for τ Ceti, with $V_{ISM} = 56 \text{ km s}^{-1}$, in order to see if any revision to the \dot{M} upper limit is required. The analysis begins with hydrodynamic modeling of the astrosphere, for models assuming different stellar mass loss rates. As in many past studies (e.g., Wood et al. 2021), the code we use is a 2.5-D axisymmetric, multi-fluid code that treats the plasma as a single fluid, but the neutral hydrogen as multiple fluids corresponding to distinct particle populations created by charge exchange in different parts of the astrosphere (Zank et al. 1996). It is crucial to note that the astrospheric models are extrapolated from a heliospheric model computed from this same code that has been proven to successfully reproduce heliospheric Ly α absorption (Wood et al. 2000). A τ Ceti astrospheric model with a solar mass loss rate would simply be the heliospheric model recomputed for a V_{ISM} changed from the solar value of $V_{ISM} = 26 \text{ km s}^{-1}$ to the τ Ceti value of $V_{ISM} = 56 \text{ km s}^{-1}$ (Wood 2018). In order to vary the assumed stellar mass loss rate, we simply vary the stellar wind density at the inner boundary.

In Figure 7, we show two models of the τ Ceti astrosphere, assuming mass loss rates of $\dot{M} = 0.03 \dot{M}_\odot$ and $\dot{M} = 0.1 \dot{M}_\odot$. The LOS to the star is 59° from the upwind direction of the ISM flow in the rest frame of the star. There are three important boundaries defined by the stellar-wind/ISM interaction: the termination shock (TS), where the stellar wind is shocked to subsonic speeds; the bow shock where the ISM flow is shocked to subsonic speeds; and between these the astropause (AP), which is the contact surface separating the plasma flows of the fully ionized stellar wind and the partially ionized ISM flow. The locations of the TS and AP boundaries are explicitly identified in Figure 7. From models like those in Figure 7, we can compute predicted H I Ly α absorption for our LOS to the star, for comparison with the data.

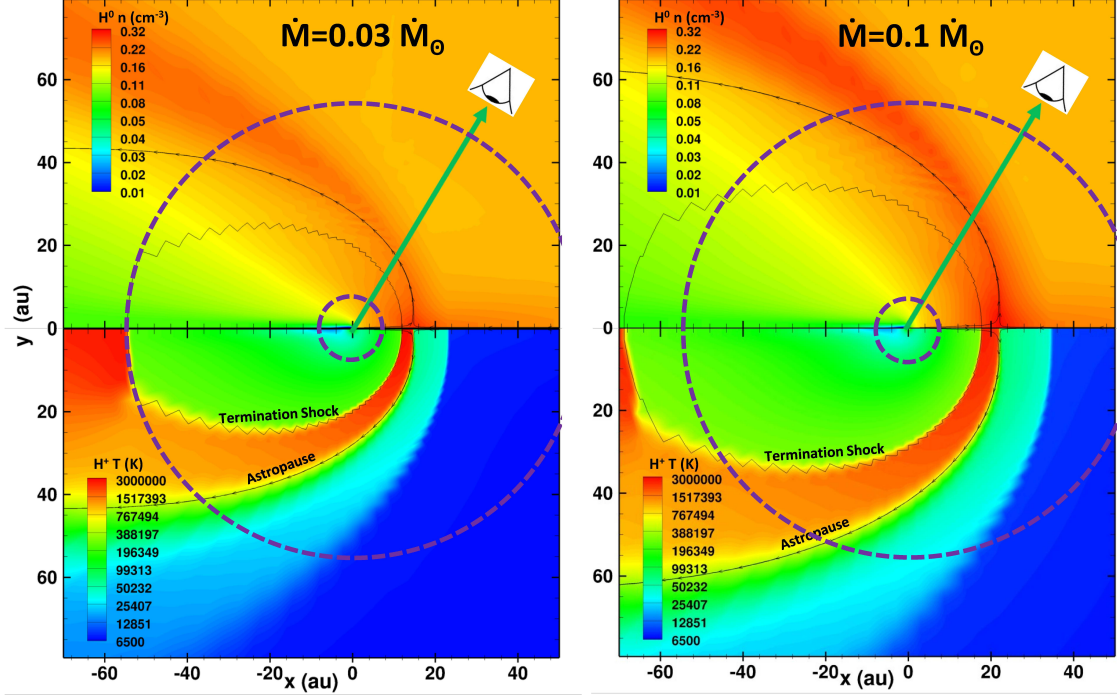


Fig. 7.— Hydrodynamic models of the τ Ceti astrosphere, assuming stellar mass loss rates of $\dot{M} = 0.03 \dot{M}_\odot$ (left) and $\dot{M} = 0.1 \dot{M}_\odot$ (right). The top panels show neutral H density and the bottom panels show proton temperature. The termination shock and astropause boundaries are labeled in the plasma temperature panel. The LOS to the star is indicated, at 59° from the upwind direction of the ISM flow. Dashed circles schematically indicate the spatial extent of τ Ceti's debris disk, demonstrating that the disk will be at least partly exposed to the ISM outside the astropause, regardless of how the disk is actually oriented relative to the astrospheric structure.

In Figure 8, this predicted absorption is compared with the observed absorption for the old τ Ceti spectrum from 2000, which is still used here because it has a much longer exposure time and therefore significantly higher S/N (see Table 1). Predicted absorption is shown for 4 models with mass loss rates ranging from $\dot{M} = 0.03 - 0.20 \dot{M}_\odot$. Because there is no actual detected astrospheric absorption, the goal is to infer an upper limit in \dot{M} based on an assessment of which models predict absorption strong enough that it should have been detected. This assessment is unfortunately rather subjective. We believe the $\dot{M} = 0.2 \dot{M}_\odot$ and $\dot{M} = 0.1 \dot{M}_\odot$ models yield absorption that should have been detectable, but we are not convinced that the $\dot{M} = 0.05 \dot{M}_\odot$ and $\dot{M} = 0.03 \dot{M}_\odot$ models yield detectable absorption. Thus, we ultimately conclude that we still infer an upper limit of $\dot{M} < 0.1 \dot{M}_\odot$, unchanged from the Wood (2018) conclusion.

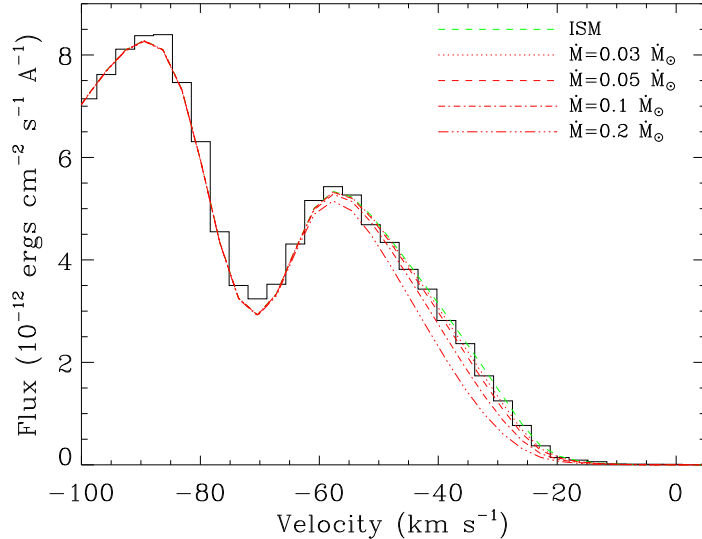


Fig. 8.— A close-up of the blue side of the H I Ly α absorption observed toward τ Ceti, with the narrow absorption at -73 km s^{-1} being ISM D I. Predicted astrospheric absorption is shown for four models assuming stellar mass loss rates of $\dot{M} = 0.03 - 0.20 \dot{M}_\odot$, leading us to quote an upper limit of $\dot{M} < 0.1 \dot{M}_\odot$ for τ Ceti.

5.2. Debris Disk Implications

Figure 7 indicates just how compact the τ Ceti astrosphere must be based on the $\dot{M} < 0.1 \dot{M}_\odot$ measurement. The TS and AP distances in the upwind direction must be less than 18 au and 22 au, respectively. These can be compared with the distances measured in our own heliosphere by the *Voyager* spacecraft, where *Voyager 1* encountered the termination shock and heliopause at distances of 94 au (Stone et al. 2005) and 121 au (Gurnett et al. 2013), respectively, and *Voyager 2* encountered the termination shock and heliopause at distances of 84 au (Stone et al. 2008) and 119 au (Burlaga et al. 2019), respectively. The compactness of τ Ceti’s astrosphere is due in part to its weak stellar wind, but is also due to the relatively high ISM wind speed in the stellar rest frame, $V_{ISM} = 56 \text{ km s}^{-1}$.

One consequence of τ Ceti’s compact astrosphere is that τ Ceti’s well-studied debris disk should be at least partly exposed to the ISM. Debris disks were first discovered around nearby stars as IR excesses in *Infrared Astronomical Satellite* (IRAS) data. Initially, the detected debris disk stars were dominated by A stars like Vega and β Pic, and a few relatively young FGK stars like ϵ Eri. An exception was τ Ceti, which was the first truly old, inactive FGK star to have a detected disk (Aumann 1985). Modern IR surveys have actually found the debris disk phenomenon to be relatively common among FGK stars. From *Herschel* observations, Montesinos et al. (2016) report a detection percentage of 23% for FGK stars within 15 pc, with no clear difference between young, active stars and old, inactive stars.

Debris disks are believed to be dusty remnants of protoplanetary disks, with the dust population continuously renewed by collisions involving planetesimals of various sizes. The Kuiper Belt

is the closest analog of this in our own solar system, but its total dust mass is well below that of the debris disk stars. A recent estimate of the solar system’s dust mass based on *New Horizons* data finds $M_{dust} = 8.2 \times 10^{-7} M_{\oplus}$ (Poppe et al. 2019). This is over two orders of magnitude less massive than τ Ceti’s debris disk, with $M_{dust} = (2.1 \pm 0.7) \times 10^{-4} M_{\oplus}$, and it should be noted that τ Ceti’s disk is the *least* massive in the debris disk survey of Holland et al. (2017). This raises an obvious question about why the debris disk masses of old FGK stars vary so much. The τ Ceti example suggests that age and metallicity are not major factors, as τ Ceti has a disk mass much heftier than that of the Sun despite being both metal poor and much older (see Table 2).

One factor that could in principle affect the dust population of debris disks is exposure to impacts from ISM dust particles. Sandblasting of larger bodies in debris disks by ISM dust could contribute to dust renewal in debris disks, or at least alter the characteristics of the dust in the disk. The possibility of ISM sandblasting affecting debris disk dust was considered in the early days of debris disk research. However, it was largely dismissed because for A stars, which account for a large fraction of detected debris disks, radiation pressure prevents the lighter ISM dust particles from coming anywhere near the star (Artymowicz & Clampin 1997), and for coronal FGK stars like the Sun, the astrospheric cocoons created by coronal winds serve the same purpose (Mann et al. 2006). Only the largest ISM dust particles can penetrate our Sun’s heliopause, and such particles are too few to be important. Thus, since the Kuiper Belt is comfortably encased inside the heliopause, ISM dust impacts should have little effect on the dust population in our own solar system.

However, these arguments against the relevance of ISM exposure do not apply to τ Ceti’s debris disk. Radiation pressure will be unimportant for a G8 V star, and we find here that τ Ceti’s astrosphere is so compact that it will not protect the disk from ISM exposure either, at least not fully. Observations from *Herschel* and the Atacama Large Millimeter/submillimeter Array (ALMA) suggest a debris disk located roughly 6 – 55 au from the star (Lawler et al. 2014; MacGregor et al. 2016). This debris disk extent is shown schematically in Figure 7. Although no attempt is made to properly orient the disk relative to the astrospheric structure and our LOS to the star in this figure, it is clear that the outermost part of the disk will be at least partly beyond the astropause regardless of orientation, and therefore exposed to the ISM. It is worth pointing out that the disk is observed roughly face-on from Earth, with a tilt angle of about $i = 35^\circ \pm 10^\circ$ from the plane-of-sky (Lawler et al. 2014). A full 3-D orientation of the disk relative to the astrosphere and LOS could in principle be inferred from this, if combined with the estimated disk position angle of $PA_{disk} = 105^\circ \pm 10^\circ$ (Lawler et al. 2014), and the position angle of the ISM flow vector in the stellar rest frame, which we infer from the stellar motion and local ISM flow vector to be about $PA_{ISM} = 96^\circ$. This is, however, complicated by ambiguity about which direction the disk is tilted relative to the plane of sky.

It is worthwhile to consider whether there are other debris disk stars with Ly α observations that indicate astrospheres compact enough for the disk to be exposed to the ISM. An astrospheric detection for a star not only indicates the size of the astrosphere, but also proves that the star

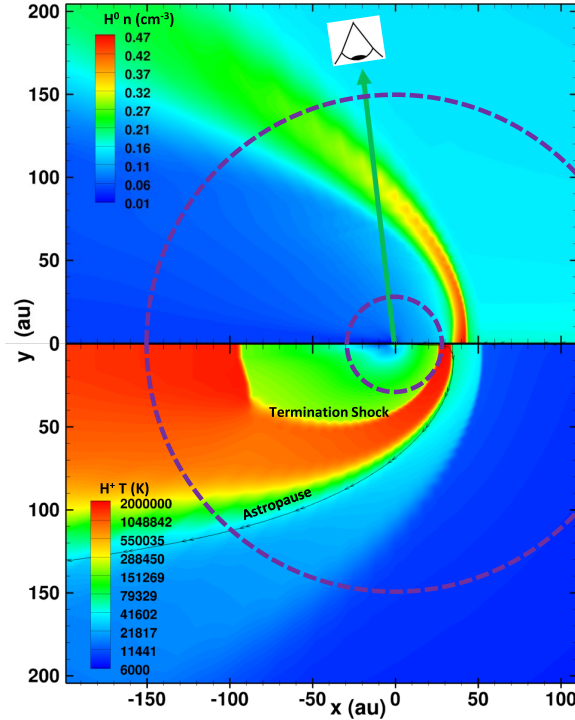


Fig. 9.— The best-fit $\dot{M} = 0.3 \dot{M}_\odot$ hydrodynamic model for the astrosphere of 61 Vir from Wood et al. (2005a) is shown, with neutral H density in the top panel and plasma temperature in the bottom. As in Figure 7, dashed circles schematically indicate the extent of 61 Vir’s debris disk, demonstrating that the disk will be at least partly exposed to the ISM.

is surrounded by ISM that is at least partly neutral, presumably containing a population of dust available to impact debris disks through sandblasting effects. This distinction is important, as much of the Local Bubble that surrounds the Sun is actually fully ionized ISM that probably lacks a significant dust constituent. We are aware of only three stars with detected astrospheric absorption that also have reported debris disks: ϵ Eri, ξ Boo, and 61 Vir (Montesinos et al. 2016; Holland et al. 2017; Wood et al. 2021). The astrospheres of ϵ Eri and ξ Boo are significantly larger than our heliosphere, and are therefore likely to be large enough to fully contain their debris disks (Wood et al. 2002, 2005a). Thus, those disks should not experience significant exposure to the ISM. This is not the case for the G5 V star 61 Vir, however, which has a weak wind of only $\dot{M} = 0.3 \dot{M}_\odot$, and which sees a high ISM wind speed of $V_{ISM} = 51 \text{ km s}^{-1}$ (Wood et al. 2005a).

In Figure 9, we show a figure analogous to Figure 7, but for 61 Vir instead of τ Ceti. The best-fit astrospheric model from Wood et al. (2005a) is replicated, and the $\sim 30 - 153$ au debris disk extent illustrated schematically (Wyatt et al. 2012; Marino et al. 2017). As is the case for τ Ceti, the outermost part of the debris disk is at least partly exposed to the ISM outside the astropause. Unlike τ Ceti, we are observing this debris disk nearly edge-on, with $i = 82^\circ \pm 4^\circ$ and $PA_{disk} = 59^\circ \pm 5^\circ$ (Marino et al. 2017). For completeness, we note that from 61 Vir’s stellar motion we estimate $PA_{ISM} = 28^\circ$.

If sandblasting from ISM dust is an important process, there should in principle be observable consequences for the debris disk properties of τ Ceti and 61 Vir. The spectral energy distributions (SEDs) of debris disks are often modeled with simple single temperature blackbodies, but with a modification factor of $(\lambda_0/\lambda)^\beta$ beyond the turnover wavelength λ_0 , in order to correct for emission inefficiencies of small grains at higher wavelengths (Kennedy et al. 2012). In SED fits, λ_0 and β can be free parameters of the fit. If dust properties in a certain population of debris disks were uniquely affected by a particular physical process, such as ISM sandblasting, this in principle might reveal itself in unusual λ_0 or β parameters.

Inspection of existing surveys does not imply any clear oddity about τ Ceti or 61 Vir in this respect (Holland et al. 2017; Sibthorpe et al. 2017). However, uncertainties in λ_0 and β are large, and the two parameters often degenerate, leading Holland et al. (2017) to simply quote wide ranges of possible values for most stars. Furthermore, for FGK stars there is also a concern that stellar chromospheres are contributing to excess emission above that of the photosphere at long wavelengths, complicating this kind of analysis even further (Villadsen et al. 2014; MacGregor et al. 2016). Theoretical modeling is needed to identify observable diagnostics of ISM sandblasting in debris disk observations, in order to test if the disks of τ Ceti and 61 Vir are demonstrably affected by this process.

Finally, besides τ Ceti, it is worth noting that there is another nearby G8 V star, HD 61005 ($d = 36.6$ pc), with a debris disk that has been proposed to be affected by ISM exposure (Hines et al. 2007; Maness et al. 2009). The unusually asymmetric appearance of this disk in HST images led to its moniker “The Moth”. Although identical in spectral type to τ Ceti, HD 61005 is different in being young and very active, and its debris disk is more massive by over two orders of magnitude (Holland et al. 2017). Interaction with the surrounding ISM is one possible way to explain the asymmetries seen for The Moth, but this would seem to require much higher ISM densities than observed around the Sun. Such high densities are very rare within the Local Bubble, but we do note that HD 61005 is located in the ring of high ISM column densities that has been interpreted as an extended compression region in the local ISM, where high ISM densities would be more likely (Swaczyna et al. 2022; Zucker et al. 2025; Youngblood et al. 2025). The debris disks of HD 32297 (A0 V) and HD 15115 (F4 IV) provide additional examples of relatively nearby disks with asymmetries that may be induced by ISM interaction (Redfield 2007; Debes et al. 2009; Bhowmik et al. 2019). However, disk shaping by massive planets with eccentric, inclined orbits is another possible way to explain disk asymmetries (Esposito et al. 2016).

6. Summary

We have presented and analyzed new HST UV spectra of HD 166620 and τ Ceti. The former represents the first UV measurements for a star established to be in an MGM phase, in which a previous clear stellar activity cycle has ceased. We compare the UV properties of HD 166620 with those of τ Ceti and HD 191408, two stars similar in both spectral type and old age. Our findings

can be summarized as follows:

1. Analysis of the stellar chromospheric H I Ly α and Mg II h & k lines requires correcting for ISM absorption, so a necessary analysis of the ISM absorption along the HD 166620 and τ Ceti lines of sight is provided.
2. We find that our MGM star, HD 166620, has H I Ly α surface fluxes significantly lower than those of τ Ceti and HD 191408, and nearly a factor of two lower than observed for the Sun at solar minimum. The Mg II h & k lines show a similar pattern only if Mg II fluxes are normalized from stellar to solar photospheric abundances.
3. The very low Ly α and Mg II fluxes for HD 166620 could in principle imply particularly low chromospheric activity for stars in MGM phases, but this conclusion is dubious since the Ca II S-index used to monitor HD 166620's activity for decades does not show S-index values in HD 166620's MGM phase that are lower than observed during stellar minima observed when the star was cycling (Baum et al. 2022; Luhn et al. 2022). Unfortunately, no UV spectra of HD 166620 are available to see if that also applies to UV fluxes at such minima.
4. The comparative chromospheric activity levels of our three old, inactive G8-K2 stars are not necessarily echoed in the transition regions or coronae of these stars. We find that it is HD 191408 that actually has the lowest transition region C IV λ 1548 flux of the three stars. And it is τ Ceti that is faintest in coronal X-ray emission, based on archival ROSAT/HRI data.
5. For τ Ceti, our new Ly α data are compared with an older observation from 2000. We find very little difference in stellar Ly α flux, consistent with τ Ceti being a flat-activity star with no known cyclic variation in activity. Our analysis of the new spectrum measures an ISM H I column density 0.06 higher than the value previously measured from the old spectrum, which is presumed to indicate the magnitude of uncertainty induced by uncertainties in the reconstructed stellar emission line profile.
6. Astropheric Ly α absorption is undetected for τ Ceti, and using new models we confirm a previous upper limit for the star's mass loss rate of $\dot{M} < 0.1 \dot{M}_\odot$, the weakest wind yet inferred from the Ly α diagnostic.
7. The τ Ceti astrosphere is compact enough that the star's debris disk must be at least partly exposed to the ISM, with potential ramifications for the dust population of the disk due to sandblasting by ISM dust grains. We note that this is also true for one other star, 61 Vir, which has both a known debris disk and detected astrosphere.

We would like to thank Dr. T. Ayres for useful discussions about STIS data processing and UV spectra of old main sequence stars. Support for HST program GO-17793 was provided by NASA

through an award from the Space Telescope Science Institute, which is operated by the Association of Universities for Research in Astronomy, Inc., under NASA contract NAS 5-26555. BEW also acknowledges financial support from the Office of Naval Research. TSM acknowledges support from NASA grant 80NSSC25K7563 and NSF grant AST-2507890. This research has made use of the SIMBAD database, operated at CDS, Strasbourg, France. All the HST data used in this paper were obtained from the Mikulski Archive for Space Telescopes (MAST) at STScI, with the specific observations available at <https://doi.org/10.17909/wtt9-z260>.

REFERENCES

Allende Prieto, C., Barklem, P. S., Lambert, D. L., & Cunha, K. 2004, *A&A*, 420, 183

Artymowicz, P., & Clampin, M. 1997, *ApJ*, 490, 863

Asplund, M., Grevesse, N., Sauval, A. J., & Scott, P. 2009, *ARA&A*, 47, 481

Aumann, H. H. 1985, *PASP*, 97, 885

Ayres, T. R., & Buzasi, D. 2022, *ApJS*, 263, 41

Baliunas, S. L., Donahue, R. A., Soon, W. H., et al. 1995, *ApJ*, 438, 269

Baliunas, S., & Jastrow, R. 1990, *Nature*, 348, 520

Baum, A. C., Wright, J. T., Luhn, J. K., & Isaacson, H. 2022, *AJ*, 163, 183

Bhowmik, T., Boccaletti, A., Thébault, P., et al. 2019, *A&A*, 630, A85

Bourrier, V., Ehrenreich, D., Allart, R., et al. 2017, *A&A*, 602, A106

Burlaga, L. F., Ness, N. F., Berdichevsky, D. B., et al. 2019, *Nature Astronomy*, 3, 1007

Charbonneau, P. 2020, *LRSP*, 17, 4

David, T. J., Angus, R., Curtis, J. L., et al. 2022, *ApJ*, 933, 114

Debes, J. H., Weinberger, A. J., & Kuchner, M. J. 2009, *ApJ*, 702, 318

Eddy, J. A. 1976, *Science*, 192, 1189

Esposito, T. M., Fitzgerald, M. P., Graham, J. R., et al. 2016, *AJ*, 152, 85

Ghezzi, L., Cunha, K., Smith, V. V., et al. 2010, *ApJ*, 720, 1290

Gurnett, D. A., Kurth, W. S., Burlaga, L. F., & Ness, N. F. 2013, *Science*, 341, 1489

Hall, O. J., Davies, G. R., van Saders, J., et al. 2021, *NatAs*, 5, 707

Hernandez, S., Monroe, T., & Carlberg, J. K. 2024, STIS Instrument Science Report 2024-04

Hines, D. C., Schneider, G., Hollenbach, D., et al. 2007, *ApJ*, 671, L165

Holland, W. S., Matthews, B. C., Kennedy, G. M., et al. 2017, *MNRAS*, 470, 3606

Judge, P. G., Saar, S. H., Carlsson, M., & Ayres, T. R. 2004, *ApJ*, 609, 392

Kennedy, G. M., Wyatt, M. C., Sibthorpe, B., et al. 2012, *MNRAS*, 426, 2115

Korolik, M., Roettenbacher, R. M., Fischer, D. A., et al. 2023, *AJ*, 166, 123

Krivova, N. A., Vieira, L. E. A., & Solanki, S. K. 2010, *JGR* 115, A12112

Lawler, S. M., Di Francesco, J., Kennedy, G. M., et al. 2014, *MNRAS*, 444, 2665

Lean, J. L., Coddington, O., Marchenko, S. V., & DeLand, M. T. 2022, *Earth and Space Science*, 9, e2021EA002211

Linsky, J. L., Wood, B. E., Youngblood, A., et al. 2020, *ApJ*, 902, 3

Luhn, J. K., Wright, J. T., Henry, G. W., Saar, S. H., & Baum, A. C. 2022, *ApJ*, 936, L23

MacGregor, M. A., Lawler, S. M., Wilner, D. J., et al. 2016, *ApJ*, 828, 113

Maness, H. L., Kalas, P., Peek, K. M. G., et al. 2009, *ApJ*, 707, 1098

Mann, I., Köhler, M., Kimura, H., Cechowski, A., & Minato, T. 2006, *A&ARv*, 13, 159

Marino, S., Wyatt, M. C., Kennedy, G. M., et al. 2017, *MNRAS*, 469, 3518

Medallion, S., Rickman, E., & Brown, J. 2023, in STIS Instrument Handbook for Cycle 32

Metcalfe, T. S., Finley, A. J., Kochukhov, O., et al. 2022, *ApJ*, 933, L17

Metcalfe, T. S., Petit, P., van Saders, J. L., et al. 2025a, *ApJ*, 986, 120

Metcalfe, T. S., & van Saders, J. 2017, *SoPh*, 292, 126

Metcalfe, T. S., van Saders, J., Pinsonneault, M. H., et al. 2025b, *ApJ*, 991, L17

Montesinos, B., Eiroa, C., Krivov, A. V., et al. 2016, *A&A*, 593, A51

Nisak, A. H., Redfield, S., Linsky, J. L., Wood, B. E., & Youngblood, A. 2025, *ApJ*, 983, 5

Owens, M. J., Lockwood, M., Hawkins, E., et al. 2017, *J. Space Weather Space Clim.*, 7, A33

Poppe, A. R., Lisse, C. M., Piquette, M., et al. 2019, *ApJ*, 881, L12

Redfield, S. R. 2007, *ApJ*, 656, L97

Redfield, S., & Linsky, J. L. 2002, *ApJS*, 139, 439

Redfield, S., & Linsky, J. L. 2004, *ApJ*, 602, 776

Redfield, S., & Linsky, J. L. 2008, *ApJ*, 673, 283

Schmitt, J. H. M. M., & Liefke, C. 2004, *A&A*, 417, 651

Schneider, A. C., Shkolnik, E. L., Barman, T. S., & Parke Loyd, R. 2019, *ApJ*, 886, 19

Sibthorpe, B., Kennedy, G. M., Wyatt, M. C., et al. 2018, *MNRAS*, 475, 3046

Stone, E. C., Cummings, A. C., McDonald, F. B., et al. 2005, *Science*, 309, 2017

Stone, E. C., Cummings, A. C., McDonald, F. B., et al. 2008, *Nature*, 454, 71

Swaczyna, P., Schwadron, N. A., Möbius, E., et al. 2022, *ApJ*, 937, L32

Tang, Y. K., & Gai, N. 2011, *A&A*, 526, A35

Taylor, A., Dunn, A., Peacock, S., Youngblood, A., & Redfield, S. 2024, *ApJ*, 964, 80

Usoskin, I. G., Chatzistergos, T., Solanki, S. K., et al. 2025, *A&A*, 698, A182

Usoskin, I. G., Mursula, K., & Kovaltsov, G. A. 2000, *A&A*, 354, L33

Usoskin, I. G., Solanki, S. K., Krivova, N. A., et al. 2021, *A&A*, 649, A141

van Saders, J. L., Ceillier, T., Metcalfe, T. S., et al. 2016, *Nature*, 529, 181

van Saders, J. L., Pinsonneault, M. H., & Barbieri, M. 2019, *ApJ*, 872, 128

Villadsen, J., Hallinan, G., Bourke, S., Güdel, M., & Rupen, M. 2014, *ApJ*, 788, 112

Wood, B. E. 2018, *JPhCS*, 1100, 012028

Wood, B. E., Linsky, J. L., Hébrard, G., Williger, G. M., Moos, H. W., & Blair, W. P. 2004, *ApJ*, 609, 838

Wood, B. E., Müller, H.-R., Redfield, S., et al. 2021, *ApJ*, 915, 37

Wood, B. E., Müller, H. -R., & Zank, G. P. 2000, *ApJ*, 542, 493

Wood, B. E., Müller, H. -R., Zank, G. P., & Linsky, J. L. 2002, *ApJ*, 574, 412

Wood, B. E., Müller, H. -R., Zank, G. P., Linsky, J. L., & Redfield, S. 2005a, *ApJ*, 628, L143

Wood, B. E., Redfield, S., Linsky, J. L., Müller, H.-R., & Zank, G. P. 2005b, *ApJS*, 159, 118

Wright, J. T. 2004, *AJ*, 128, 1273

Wu, C. -J., Krivova, N. A., Solanki, S. K., & Usoskin, I. G. 2018, *A&A*, 620, A120

Wyatt, M. C., Kennedy, G., Sibthorpe, B., et al. 2012, *MNRAS*, 424, 1206

Youngblood, A., France, K., Koskinen, T., et al. 2025, *AJ*, in press

Youngblood, A., Pineda, J. S., Ayres, T., et al. 2022, *ApJ*, 926, 129

Zank, G. P., Pauls, H. L., Williams, L. L., & Hall, D. T. 1996, *J. Geophys. Res.*, 101, 21639

Zucker, C., Redfield, S., Starecheski, S., Konietzka, R., & Linsky, J. L. 2025, *ApJ*, 986, 58